19 pages

TRI-PP-89-102
Nov 1989

Absolute differential cross sections for $\pi^{\pm}p$ elastic scattering at $30 \leq T_{\pi} \leq 67$ MeV

J. T. Brack,* R. A. Ristinen, J. J. Kraushaar, R. A. Loveman,† and R. J. Peterson

Nuclear Physics Laboratory, Department of Physics, University of Colorado, Boulder, Colorado 80309-0446

G. R. Smith, D. R. Gill and D. F. Ottewell

TRIUMF, Vancouver, British Columbia, Canada V6T 2A3

M. E. Sevior and R. P. Trelle

University of British Columbia, Vancouver, British Columbia, Canada V6T 2A3

E. L. Mathie

University of Regina, Regina, Saskatchewan, Canada S4S 0A2

N. Grion and R. Rui

I.N.F.N. and University of Trieste, Trieste, Italy 34127

Abstract

Absolute $\pi^{\pm}p$ differential cross sections have been measured at incident pion energies of 30.0, 45.0, and 66.8 MeV, using active targets of scintillator plastic ($CH_{1.1}$) to detect recoil protons in coincidence with scattered pions. Statistical uncertainties are typically $\pm 3\%$; systematic uncertainties are $\pm 2\%$. The results are consistent with two earlier measurements by this group employing different experimental techniques at 67 MeV and higher incident pion energies. The $\pi^{-}p$ cross sections are in good agreement with currently accepted phase-shift analyses, but the corresponding $\pi^{+}p$ predictions are typically 15% higher at large angles than the $\pi^{+}p$ data reported here.

(submitted to Physical Review C)

PACS 25.80.Dj

*Now at TRIUMF, Vancouver, British Columbia, Canada V6T 2A3
†Now at SAIC, Santa Clara, CA 95054

I. INTRODUCTION

Pion-nucleon scattering data form the basis of our knowledge of one of the most fundamental interactions involving strongly interacting particles. In the past, these data have provided a proving ground for isospin conservation, analytic continuity of scattering variables, resonance phenomena, and models of meson exchange forces. Scattering data provide the basis for calculation of the πN form factor which is a crucial ingredient in calculation of other seemingly unrelated processes involving nucleons, such as eN scattering where it enters as part of the nucleon form factor. The πN cross sections also have implications for systems containing many nucleons since virtually all data from π-nucleus experiments using magnetic spectrometers are normalized to the "known" π-nucleon cross sections through the use of a proton target. Thus imprecise knowledge of $\pi^{\pm}p$ differential cross sections may compromise our understanding of the way in which pions interact with nucleons in a nuclear environment.

Beyond these concerns, recent publications have heightened interest in the precise behavior of the low energy πN phase shifts and their extrapolation to threshold. The theoretical value of the πN σ term, as extracted from the QCD Lagrangian through the use of chiral symmetry, is supported by data from pionic atom studies, but not by existing $\pi^{\pm}p$ elastic differential cross-section data,[1] and one criticism is that these latter data are in such disarray that no sufficiently precise extrapolation can be made. The σ term has been related to the $s\bar{s}$ quark content of the proton.[2] A substantial strange quark content of the proton, as suggested by the πp differential cross section data, would be of serious importance to the quark model of the nucleon. As noted at a recent conference,[3] if the strange quark content of the nucleon is large, lattice calculations using the quenched approximation (in which the strange quark content of the nucleon is zero) will fail to reproduce the physical nucleon mass, the SU(2) Skyrme model will be unreliable, and kaons may condense in nuclear matter of rather low density.

Further, there may be independent support for a large $s\bar{s}$ content: the EMC group has recently reported results[4] of measurements of the spin asymmetry in deep inelastic lepton scattering. These results indicate that the spin-dependent structure function for the proton does not agree with calculations based on the quark model, and that the spin of the constituent quarks may have little to do with the spin of nucleons.[4] One explanation that has been proposed is that the spin carried by a possible $s\bar{s}$ content of the nucleon cancels that of the u and d quarks, and that gluons and orbital angular momentum make up the spin of the nucleon.[5]

It has been argued that the existing $\pi^{\pm}p$ differential cross section data near and above the πp $\Delta(1232)$ resonance establish the energy dependence of the πN partial-wave phase shifts, and are therefore a sufficient base for extrapolation via dispersion relations to the correct phase shifts below resonance and down to threshold energies. However, a single data set[6] represents the entire SP89[7] differential cross-section data base near resonance, and there is considerable disarray at lower pion bombarding energies where those measurements overlap other experiments in energy and angle. Although the $\pi^{\pm}p$ experiment reported here does not constitute a definitive σ term measurement, it will contribute to the precision with which the above-threshold phase shifts are known, and thus to the necessary extrapolation.

The purpose of the experiment described here and of two previous experiments by largely the same experimental group[8,9] is to establish a reliable data base by precise measurement of absolute $\pi^{\pm}p$ differential elastic cross sections over a range of energies below the delta resonance. Although no fewer than three previous experimental groups[6,10,11] have set out with the same purpose, discrepancies of 20% still exist in this kinematic region while stated experimental uncertainties are in the 2–4% range.

The laboratory and experimental technique used for the measurements reported here were chosen to maximize the reliability of the results. The pion beam provided by a cyclotron-based

meson factory is especially well suited to absolute measurements. The 23 MHz rf frequency of the TRIUMF cyclotron provides an essentially dc pion beam and, therefore, reliable pulse-height and time-of-flight (TOF) information are available from in-beam scintillators. TOF information can be used to separate pions from muons and electrons, while pulse-height information can be used to reject protons and identify rf buckets which deliver multiple particles to the experimental target. Thus each particle incident on the target is counted directly, and beam normalization corrections for muon and electron contamination are very accurate. The end result, considering both pion fraction and multiples, is an absolute beam normalization known to better than 1%.

The ability to perform coincidence experiments at incident pion energies below 100 MeV is the primary technical advantage of the solid targets used in this experiment over the liquid targets previously used. All previous measurements of $\pi^{\pm}p$ cross sections below 143 MeV (except that of Ref. 8) used only a single-arm detection apparatus because recoil protons at these energies lose excessive energy while exiting the LH_2 target structure. The use of thin solid targets allows detection of coincident recoil protons outside the target (see Ref. 8), or in the case of the active solid target experiment reported here, within the target itself, providing a distinct signature of πp elastic scattering without the uncertainties involved in a large background subtraction process. The solid plastic targets also simplify evaluation of experimental uncertainties in the number of scattering nuclei in the target. Physical measurements and chemical analysis of the target material are each good to 1%, giving an overall target-associated normalization uncertainty of about 1.5%.

II. METHOD AND APPARATUS

The experiment was performed on the M13 channel[12] at TRIUMF using incident pion kinetic energies of 30.0, 45.0 and 66.8 MeV at the center of the scattering target. The target was viewed by six pion counter telescopes, each of which consisted of two plastic scintillators as shown in Fig. 1. The beam spot size on the target was determined by the scintillation counter S, and coincidences of S with the target signal counted the incident beam. The details of the active target technique, beam monitoring, and pion detectors are presented in the following subsections.

A. Active target

An active target provides a means of detecting the recoil target nucleus in coincidence with the scattered particle, thereby establishing that the detected scattering event occurred in the target. The technique is not an alternative to the use of LH_2 targets for all πp elastic scattering measurements; at the incident pion energies considered here it is not useful, for instance, at laboratory scattering angles smaller than about 20° or larger than about 140°. For each elastic scattering event, the target signal is the sum of the light produced in the scintillator by the pion before and after the scattering and the light produced by the recoil particle. The fluorescent response (light signal produced relative to kinetic energy loss) of the target scintillator is typically quite different for the passing pion and the stopping recoil particles, and is also quite different for the recoil proton and the recoil carbon nucleus, as shown in Fig. 2.

For the purpose of anticipating the relative amplitudes of the light pulses produced by the various particles, the relative light output for the passing pion and a stopping proton was derived from the empirical relationship given by Madey *et al.*,[13] which compares the response of various organic scintillator materials to stopping protons and electrons. For the particle energies in this work, it is a reasonably good approximation to take the light output of a passing pion to be identical to that of an electron for the same energy loss. It may be shown,

for example, that a 1 MeV stopping proton produces light equivalent to that of a 0.2 MeV pion energy loss, a 5 MeV stopping proton produces light equivalent to that of a 2 MeV pion energy loss, and a stopping proton of 40 MeV creates light equivalent to that of a 30 MeV pion energy loss.

The light produced in a scintillator by recoil carbon and hydrogen ions can be described as a function of the ion range in the scintillator, with particles of greater range producing more light.[14] For incident pions of a given energy scattered at a given angle from an organic scintillator, the light output of a recoil proton will be more than a hundred times greater than that produced by a recoil carbon nucleus, as shown in Fig. 2. The carbon atom recoiling from a pion scattering event produces negligible light for the purpose of establishing the position of the carbon recoil peak in a target pulse-height spectrum. The carbon peak therefore appears at a position very nearly corresponding to that of the light produced by the pion as it passes through the target, and the proton peak appears at an appreciably larger amplitude corresponding to the summed light outputs of the pion and the stopping proton. The dominance of the carbon peak by the pion light output results in its high energy side having the Landau shape expected for the passing pion signal, as seen in Fig. 3. The Landau tailing is less apparent on the proton peak for the higher recoil proton energies, but it becomes more noticeable at smaller pion scattering angles and lower incident pion energies where the proton light output is not so large relative to that of the passing pion.

In the present method the angular orientation of the target relative to the incident beam was chosen to minimize the probability that the recoil protons associated with detected pions would escape from the target before coming to rest. A typical target orientation is shown in Fig. 1. For any one pion scattering angle a target angle can be chosen such that the recoil proton trajectories lie exactly in the plane of the target (neglecting multiple scattering), but for a situation involving detection of pions over extended scattering angles, a balance must be struck between proton escape through the downstream surface and through the upstream surface of the target. The former events correspond to the more backward scattered pions from interactions in the target volume near the downstream surface and the latter events correspond to the more forward scattered pions from interactions in the target volume near the upstream surface. Such losses of recoil protons effectively reduce the target thickness by an amount which depends on the incident pion energy, the pion scattering angle, and the target angle. For the purpose of selecting a target angle, it is assumed that a recoil proton will escape if its kinematically defined trajectory lying within the target volume is shorter than the known range of a proton having the same energy. For the six-arm example depicted in Fig. 1, the target angle has been selected to minimize the total number of protons which escape from the target in coincidence with detected pions, calculated under the simplifying assumption of isotropic πp scattering. As a practical approximation for this six-arm setup, one may achieve good results by setting the target plane to correspond to the proton scattering angle for pions detected in the next-to-most-backward pion counter arm.

Figure 3 displays a spectrum of the target pulse amplitude for one pion counter arm. This figure shows a peak of πp elastic events, a large peak due to pion-carbon elastic scattering, and a continuum of events primarily caused by energetic protons from pion absorption on carbon. The products of this absorption process can produce a range of pulse heights in the target in coincidence with a proton being detected in a pion arm. There is also a small continuum of events distributed between the proton and carbon peaks due to proton escape from the target surface. Because of the much larger scattering cross section for carbon, the carbon peak is many times larger than the proton peak. If the beam rate is sufficiently high, a satellite peak will appear on the high-energy side of each of the main two peaks because of the probability of a second pion passing through the target in the same cyclotron rf cycle which included the scattered pion, and having its light output added to that of the scattering event. Such peaks are not visible in Fig. 3, where a beam rate of about 1 MHz was used,

corresponding to a 2% probability of a second pion in a given rf cycle. These doubles peaks may be removed by a software veto on the doubles-amplitude pulse heights in one of the beam-defining counters.

For a given incident pion energy, scattering angle, and target angle, a thinner target will give better separation of the carbon peak and the proton peak. Although the centroid-to-centroid separation of the two peaks is independent of target thickness, both peaks have widths proportional to the square root of the light output, and so become more narrow as the energy deposited by the pion is reduced. Thus a thinner target will permit measurements at more forward angles where the recoil energy is small and where the proton peak is less well separated from the carbon peak. The problem of resolving the proton peak from the carbon peak rapidly becomes more severe as the recoil proton energy drops, because of the dramatic reduction in the fluorescent response for protons at low energies. The minimum achievable scattering angle is determined by the ability to resolve the carbon and proton peaks when using a narrow channel momentum width and a narrow pion counter angular acceptance, and with a target sufficiently thin that the linewidth is not broadened significantly by deposited pion energy. In this case the amplitude of the proton signal will be determined primarily by the light produced by the recoil proton, with only a minor contribution from the passing pion, and the linewidth will be very nearly that of the scintillator response to monoenergetic protons. For an extended pion counter angular acceptance, the energy width of the proton recoil peak will be dominated by the $dE/d\theta$ given by scattering kinematics. The maximum achievable scattering angle is limited by the longer pion paths in the target which are experienced as the scattering angle increases and the incident and exit pion trajectories become more nearly tangent to the target surface when the target plane is oriented along the path of the recoil proton. For a given incident pion energy and scattering angle, the maximum target thickness is set by pion energy losses and the need to separate the two peaks; the minimum useful target thickness is set by the need to keep the proton escape correction down to a small value.

In the present experiment, the target-scintillator was of Bicron BC412 material,[15] 12.7 cm square. Target thicknesses and densities were determined using a micrometer and a balance, and the manufacturer's C/H ratios were confirmed by measurements performed at two independent analytical laboratories[16,17] (see Table I). Several methods were used to evaluate the effects of loss of recoil protons from the targets (see below), including the simultaneous use of two such targets of different thicknesses mounted back-to-back with a light shield and graphite proton absorber between them, in a sandwich configuration. In order to optimize timing and light collection, each target was viewed by two photomultipliers through adiabatic lightpipes, one connected to the top edge and one to the bottom edge. The assembly was aligned and centered at the beam focal point to an accuracy of $\pm 0.3°$ and ± 2 mm.

B. Beam monitoring

The beam spot on the target was defined by a 40 mm wide by 47 mm high by 1.6 mm thick scintillator, S, 25.8 cm upstream of the target (see Fig. 1). The cross-sectional area of the beam at the target was smaller than S due to the focusing effects of the channel. For runs necessitating a large target angle, a smaller scintillator was used for S which was only 20 mm wide and ensured that the beam spot was in the central region of the target. The number of beam particles incident on the target was determined by scaling coincidences of the S counter and target signals, subject to an upper-level discriminator setting $\overline{S}$, to remove possible beam protons.

C. Pion counters

The target was viewed by six pion counter telescopes, each consisting of two 0.3 cm thick plastic scintillators, $\pi 1$ and $\pi 2$ in Fig. 1, which ensured that scattered pions detected in each

telescope originated in the target region. These counter arms were typically spaced 10° apart. Each $\pi 1$ counter was viewed by a single RCA 8575 photomultiplier via a 90° lucite lightpipe. Two such photomultipliers were used for the $\pi 2$ counters, one attached above and one below the scintillator. The telescopes were mounted on a machined table and the angular location of the telescopes on the table was accurate to better than ±0.25°. The $\pi 1$ counters were 9.0 cm wide by 20.0 cm high, large enough to intercept all straight line paths from the target to the $\pi 2$ counters, and were placed at a radius of 65.5 cm from the target center, although this distance was varied during several runs as a check on our ability to reproduce multiple scattering and decay effects by Monte Carlo simulation (see below). The $\pi 2$ counters were 9.0 cm wide by 30.0 cm high and were placed at a radius of 123.8 cm from the target, defining a geometric solid angle of 17.6 msr per counter. Data were gathered simultaneously in the six pion counter telescopes. Events in a given arm were defined to be coincidences of $\pi 1 \cdot \pi 2$. The efficiency of these counters is discussed below.

III. ANALYSIS

All events having coincidences Beam · Arm, or $[S \cdot \bar{S} \cdot T] \cdot [\pi 1 \cdot \pi 2]$, were recorded on tape for analysis. Several criteria and corrections were applied to signals creating coincidences defined by the bracketed expressions, as described below.

A. Scattered pion data

If a πp elastic scattering event has occurred in the target, the target signal represents the summed light output of the recoil proton and the pion as it enters the target and scatters out, and is distinct from that of a πC elastic or inelastic event. In addition, pions scattered from elastic interactions in the target have a distinct TOF between the target and $\pi 2$ counter. These cuts can be made on a 2-dimensional plot of target pulse-height vs. TOF to the $\pi 2$ counter (see Fig. 4).

Some energetic protons originating from pion absorption in the target have nearly the same TOF to the $\pi 2$ counter as elastically scattered pions, and some of these three (or more) body final states may also generate the same light output in the target as that of a πp event. To separate these energetic protons from the elastic pion events, a further requirement could be proper $\pi 2$ pulse height. This additional restriction can be made on a dot plot of $\pi 2$ TOF vs. $\pi 2$ pulse height by requiring the events to fall inside a box defining the elastic pion region. In principle, energy loss and TOF are redundant, since each is a measure of particle velocity. Indeed, yields were found to be identical with and without this cut. The main purpose of this cut was to clean up the the target pulse height vs. $\pi 2$ TOF dotplots, described above, from which yields were extracted.

In the absence of the $\pi d \rightarrow 2p$ reaction on quasi-deuterons in the carbon content of the target, the dotplots described above provide a clean method of data extraction. However, this absorbtion reaction is present for positive pion beams, and at lower incident pion energies it forms a continuum under the πp events on the dotplots. At 67 and 45 MeV this background was negligibly small, and dotplots were used for data extraction. At 30 MeV the absorbtion background was large for π^+ and a different method of data extraction was necessary. The 30 MeV $\pi^+ p$ yields were taken from histograms of the target pulse height spectra (see Fig. 5). The background was fit in two regions, to the left and right of the $\pi^+ p$ peak, and a smooth curve connecting these fits was drawn under the peak. The area above this curve was integrated and used as the yield. In order to test and justify the use of the histogram method, selected box cut method yields from the 30 MeV $\pi^- p$ and 45 MeV $\pi^+ p$ analyses were reproduced by the histogram fitting technique. The agreement was excellent (±1%).

No separate empty target subtraction was necessary, since the requirement of the proper recoil signal in the target eliminated possible background events. If such events were contributing to the measured yields, they would be eliminated by the subtraction in the dual target technique described below. Also eliminated by this dual target technique would be any loss of events due to possible dead surface layers on the target. The agreement of the dual target and single target cross sections is evidence that these effects do not contribute to cross sections obtained with the active target method.

B. Beam counting

Signals from the in-beam scintillator S, in coincidence with the target signal, were used to count each particle incident on the targets and to define incident pion flux. Particle identification occurred at the S scintillator through TOF and pulse height techniques.

The majority of the beam protons were removed in the channel by a degrader placed between the first and second bending magnets, and the few remaining at S were removed with an upper-level discriminator, $\bar{S}$. There are typically about 10 protons per pion in the π^+ beam depending on beam energy, and none in the π^- beam, so that even a small percentage of protons passing $\bar{S}$ could increase the counted beam and lower the $\pi^+ p$ cross sections relative to those for $\pi^- p$. However, for the channel tunes used in this experiment, any protons passing through the channel have too low an energy to pass through 40 cm of air and 1.6 mm of scintillator (S) and still reach the target, which is in coincidence with S in the beam definition.

Corrections to the counted raw incident beam flux can be placed in three categories: corrections for μ and e content, corrections for two or more particles arriving simultaneously at the target, and corrections for pion decay after counting at S, but before hitting the target. In order to separate beam pion and doubles fraction determinations from scattering data acquisition, a separate circuit was arranged to sample the beam content at periodic intervals throughout the data acquisition period. This samples circuit opened the event gate until the next beam particle arrived, and all the data words for this event were written to tape with a pattern unit tag to identify it as a beam sample event. Sample event data were typically gathered at about 1% of that of the real event rate.

Muons and electrons originating at the pion production target were separated from the beam pions by TOF through the channel. A timing signal from the S counter started a time-to-digital converter, which was stopped by a delayed signal from a capacitive probe placed near the production target which sensed the primary beam from the cyclotron. These sample data were used in replay to produce histograms from which the proportion of pions could be extracted. The pion fraction of the beam at S was defined as

$$f_\pi = \frac{\pi}{\pi + \mu + e} .$$

The only exception to this was at 30 MeV π^-, where the large number of electrons was well separated by TOF, and was easily eliminated online by a hardware cut. For replay analysis of these few runs,

$$f_\pi = \frac{\pi}{\pi + \mu} .$$

A small correction to f_π was applied to account for muons from decay of pions between the last bending magnet and the S counter. These muons have nearly the same TOF through the channel as the pions, and so are not removed by the f_π cut. This correction was computed by Monte Carlo methods, and was typically 0.5%.

In addition to these corrections for f_π, a correction was applied to account for decay of pions after triggering S, but before entering the target. Some muons resulting from pion decay

between S and the target never hit the target, and therefore do not trigger either a beam coincidence or an event, so that the correction is for a smaller path length near the target, from which decay muons will hit the target. This correction was calculated by Monte Carlo methods, and varied from 2.4 to 3.3%.

Once the number of S counter signals representing pions was determined, a correction for multiple pions in a single rf beam bucket was necessary. For a cyclotron operating at 23 MHz, producing pions at a rate of 1 MHz, a probability of any one rf cycle producing a pion (P_1) is approximately 1/23. The relative probability of producing two pions (P_2) in a single rf pulse was calculated using Poisson statistics. Regardless of how many particles were present in a single rf bucket, the S counter registers a single count i.e., $S = s + d + t + ...$, where s, d, t represent the number of single-, double-, triple-pion rf buckets. Then the real number of pions passing S is

$$\begin{aligned} \text{Beam} &= s + 2d + 3t = S\left[\frac{s + 2d + 3t}{s + d + t}\right] \\ &= S\left[\frac{P_1 + 2P_2 + 3P_3}{P_1 + P_2 + P_3}\right], \end{aligned}$$

where the probability of four or more pions in a single beam burst has been ignored. The multiples fraction of the beam, f_d was defined as the term in brackets. If x is the ratio of pion rate to rf (about 1/23) then P_1, P_2 ... are known from Poisson statistics to be:

$$P_n = \frac{x^n}{n!}e^{-x}.$$

This calculation was done during replay for each run in the experiment, and f_d was typically 2%.

C. Monte Carlo simulations

Although the cuts detailed above extracted the πp events from the raw data, they did not account for loss of coincidences due to multiple Coulomb scattering of particles in the target or in air, in-flight decay of pions from πp scattering in the target, or for gain of coincidences due to in-flight decay of pions scattered at some angle outside of the cone defined by the $\pi 2$ counter, resulting in muons which hit $\pi 2$ and caused a coincidence. Further, for this active target experiment, the recoil particle signal in the target was part of the event definition, but some of these signals were lost because the scattering event occurred near the surface of the target and the recoil particle escaped from the scintillator before depositing its full light output. This loss due to escape was influenced by multiple scattering of the recoil particle, making corrections difficult to calculate directly. Monte Carlo techniques were used to determine corrections due to the above occurrences, using the GEANT Monte Carlo program.[18]

With this program, particles were originated 30 cm upstream of the target, with initial conditions chosen to simulate those in the actual experiment. The initial x and y location of each particle was chosen at random from a Gaussian distribution, roughly 2 cm wide by 3 cm high. The component of the trajectory in the x and y directions was chosen similarly from Gaussian distributions corresponding to the 1° horizontal and 2° vertical convergence of the beam. For the z direction, $\frac{\delta p}{p}$ was chosen at random from a Gaussian distribution representing the the 1% momentum bite used in the actual experiment.

Using these initial conditions, the program stepped pions through each element of the experiment (air, S, air) to the target. The S counter defined the simulated beam spot on the

target. The step length was chosen according to the atomic number and density of the material being traversed. Energy loss, Coulomb multiple scattering, decay, and nuclear interaction probabilities were calculated for each step. On reaching the downstream surface of the target, the trajectory was stopped, and a point along the path in the target was chosen at random to be the πp vertex. The pion scattering angles were chosen at random within the bounds of a defined Monte Carlo solid angle, which generously enclosed the entire six-counter array. Pions were then stepped through the remaining experimental elements (target, air, possibly $\pi 1$, possibly $\pi 2$) until they exited the experiment volume (a cube, 3 m on a side, with the target at the center). All decay and nuclear interaction products were tracked in a similar fashion. As pions pass through the experimental setup, they may or may not cause an event as defined by the counters. Then the effective solid angle for each pion counter telescope is

$$d\Omega_{\rm eff} = \frac{n}{N} d\Omega_{\rm MC},$$

where n is the number of events in that telescope, N is the total number of particles thrown, and $d\Omega_{MC}$ is the Monte Carlo solid angle into which scattered pion trajectories were allowed.

As an independent check on our ability to simulate the experiment properly using the GEANT routine, effective solid angles were also generated for one six-arm setup using the REVMOC Monte Carlo routine.[19] Effective solid angles were calculated for one counter telescope at a time. The effective solid angles calculated by the GEANT routine were found to be within one percent of those of the REVMOC routine.

For the GEANT simulations, N was typically 5×10^5 and $d\Omega_{\rm MC}$ was often as large as 2 sr, although these numbers varied widely with the energies of the scattered pions. In all cases, the code was run until approximately 10,000 simulated events had been accumulated at each scattering angle, and the resulting statistical error was therefore taken to be 1% for each of the effective solid angle and target surface loss corrections.

In addition to determining the effective solid angle for the scattered pions, the GEANT program was used to track the recoil protons to determine whether they escaped from the target. The percentage of protons escaping was used as a correction to the target thickness to give an effective target thickness, as described in the next section.

SYSTEMATIC TESTS

A. Loss of recoil protons

Because the use of an active target to detect recoil particles was a new technique, considerable effort was expended to evaluate systematic uncertainties. In particular, the loss of coincident recoil particles through the surfaces of the target could mean the loss of events. For a given incident pion energy, the fraction of escaping particles is a function of target thickness (T), target angle relative to the incident beam (ϕ) and proton recoil angle (α). If there were no multiple scattering of the recoil protons, and if their range as a function of energy (R_p) were precisely calculable, the escape fraction could be expressed (in two dimensions) as

$$f_{esc} = [R_p \sin(\phi - \alpha)]/T \ ,$$

i.e., the ratio of the target thickness from which protons can escape to the total target thickness. The fraction of protons in the target that were undetected due to nuclear interactions was treated separately.

To evaluate the effect of the escape fraction on the measured cross section, each of the variables T, ϕ, and α was varied in separate runs. The ability of the GEANT Monte Carlo routine to provide escape fractions which produced consistent cross sections for all the various geometries indicated that the correction was being made correctly. For example, for 45 MeV

incident positive pions, data were taken in separate runs using 4 different target angles, two targets of different thicknesses, and three overlapping sets of pion scattering angles. The escape fractions generated by the Monte Carlo routine for several of these conditions are shown in Fig. 6, and the resulting cross sections are displayed in Fig. 7. The effective target thicknesses varied by more than a factor of two, and f_{esc} nearly cancelled entirely for the dual target setup, described below, yet the three resulting sets of cross sections agree within about 2% at each angle. Results for the target angle tests are shown in Fig. 8. The surface escape correction generated by the Monte Carlo code for these target angles varied by as much as a factor of ten at a 90° pion scattering angle (see Fig. 6), yet the resulting cross sections from the separate modes are in agreement to ±3%. The excellent agreement of the Monte Carlo-corrected cross sections from these widely varying experimental geometries supports the estimated 1% uncertainty in these corrections. Only data from near-optimum configurations were used in the final analysis.

A dual active target method was used as a check on the ability of the Monte Carlo routine to generate the correct surface escape fractions. These measurements were made using two targets simultaneously, of thickness T_1 and T_2, set at the same angle in a sandwich configuration. The difference between the observed yields, Y_1 and Y_2, produced a differential cross section

$$\frac{d\sigma}{d\Omega} = k\frac{(Y_1 - Y_2)}{(T_1 - T_2)} ,$$

with k a constant containing the beam and target parameters. The recoil proton escape frequency was the same from the surface of either target and thus subtracted out, but at some cost in statistical precision. As a final check on our ability to resolve the surface effects, the angle of the sandwich target was varied while keeping the remainder of the setup untouched.

The equation above holds as written only if the beam energy is the same at the center of each target. At these comparatively low incident energies the difference in energy at the centers of the two targets was typically about 3%. This means that for a given pion scattering angle, the range of the recoil protons in the two targets was not precisely equal. This affected the number of protons lost through the target surface, so that the term T_1-T_2 required correction. Further, because of the incident pion energy difference and the fact that the scattered pions from the two targets traversed different thicknesses of target material, the scattered pions from the two targets exited the dual target with differing energies. This means that the effective scattered pion counter solid angle differed for the two targets, and could not be factored into the term k, so the term Y_1-Y_2 needed correction. Finally, the $\pi^{\pm}p$ cross sections in this energy region are energy dependent, and Y_2 was gathered at the lower T_π, so Y_2 was corrected for the known energy dependence of the cross section. The resulting equation corresponding to the pion energy at the center of the first target is

$$\frac{d\sigma}{d\Omega} = k\frac{[Y_1/d\Omega_1 - (Y_2/d\Omega_2 + \frac{1}{\frac{d\sigma}{d\Omega}}\frac{d\frac{d\sigma}{d\Omega}}{dT}\Delta T_\pi)]}{(T_1 - \delta T_1) - (T_2 - \delta T_2)} .$$

The terms δT_1 and δT_2 represent the surface layer thicknesses of the targets from which protons may escape. The energy dependence of the differential cross sections used in the analysis was obtained from the SAID[7] routine. The effective solid angles, $d\Omega_1$ and $d\Omega_2$, were computed using Monte Carlo methods. The cross sections extracted using this dual active target method are in agreement with those of the single active target method (see Fig. 7).

B. Detector geometry

The effective solid angle was found to be heavily dependent on the geometry for the six pion telescopes, which was varied widely during this experiment (see Table II). For geometries

in which the $\pi 1$ and $\pi 2$ counters were placed back-to-back, the ratio of Monte Carlo effective solid angle to the geometric solid angle was within a few percent of unity, reflecting the fact that the number of pions scattering out of the counter acceptance cone (or decaying to muons which leave the cone) was nearly equal to the number gained by scattering (or decaying) into the cone. Pions lost by decay and out-scattering could come only from within the cone defined by the solid angle of the counter, but in-scattered particles could come from anywhere inside a region defined by this cone plus the opening angle for the decay muon. The use of counter geometries in which the $\pi 1$ and $\pi 2$ counters were separated and formed a true telescope limited the possibilities for scatter-in, but at the expense of larger effective solid angle corrections.

Tests of the effects of the detector geometry on the measured cross sections were performed at incident pion energies of 45 and 30 MeV. At 45 MeV, two geometries were used, one in which the radii of the $\pi 1$ and $\pi 2$ detectors from the scattering target were approximately equal, and one in which these radii differed by nearly a factor of two (see Table II). Data were gathered at nine pion scattering angles using each geometry. At 30 MeV, the geometry of two telescopes was changed during a test run, so that a single run incorporated three different geometries simultaneously. A separate 30 MeV run used a single geometry for all six arms. For each of the angles at 45 or 30 MeV, cross sections resulting from the various configurations agreed within statistical error, and no systematic trend was observed with detector geometry.

C. Counter efficiency

In a separate set of tests, the efficiency of a counter telescope was checked. The counter telescope was placed directly in a 77 MeV/c incident beam (20 MeV pions) from TRIUMF's M13 channel. A small scintillator S1 (20 mm wide × 30 mm high × 1.6 mm thick) was placed 3.5 cm upstream from the center of the $\pi 1$ counter, and a second scintillator S2 (40 mm × 40 mm × 1.6 mm thick) was placed downstream of the $\pi 2$ counter. Coincidences of $S1 \cdot S2$ and of $S1 \cdot (\pi 1 \cdot \pi 2) \cdot S2$ were scaled separately and the efficiency, defined as

$$\epsilon = \frac{S1 \cdot \pi 1 \cdot \pi 2 \cdot S2}{S1 \cdot S2} ,$$

was calculated. Beam particles were separated by pulse height analysis and time of flight through the channel to the S1 counter.

The value of ϵ was 0.999 for both pions and muons, with uncertainties of 0.5% and 1.0%, respectively for the two particle types. Identical results were obtained for both positive and negative beam polarities. No change in the results was observed when the beam spot was moved from the center of the $\pi 1$ and $\pi 2$ counters to the upper ends. Additional tests checked the efficiency of a single 3.2 mm thick $\pi 1$ scintillator counter, using beam momenta as low as 54 MeV/c (10 MeV pions). The combined efficiency for pions and muons was found to be 0.999 with an uncertainty of 0.5% for both positive and negative polarities.

In the analysis of the data reported in this paper, the combined efficiency of the counter telescopes and coincidence circuit was taken to be 1.000 ± 0.005 at energies of 20 MeV and above. This range covers all energies of scattered pions for which data are reported here.

D. Beam particle identification

A second method used to deal with the doubles content of the beam was to examine in the analysis only events generated when a single pion traversed the target. To this end, test analyses were made in which all events above a cut on the S pulse height spectrum were removed from the analysis. This cut was made low enough to eliminate the entire doubles

peak, and therefore also removed a sizable fraction of the singles events as well (about 15%), so the method sacrificed statistics. Use of this method required that the above doubles correction be replaced by the appropriate fraction to represent only the number of single pion rf buckets used in the analysis, or

$$Beam \rightarrow Beam \cdot \left[\frac{Singles}{Total}\right],$$

where *Singles* and *Total* were obtained from the gated and total counts in the S pulse height spectrum, respectively. This technique was used as a check.

Less than 1% changes in the resulting cross sections were observed as the method of doubles correction was varied, except at the smallest θ_π where the separation of carbon and proton elastic events is least satisfactory on the dotplots of target pulse height vs. $\pi 2$ TOF. At these angles, the presence in the target of a second passing pion during carbon elastic events was enough to boost the target light output to approximately the equivalent of a proton elastic event. The effect was largest for thicker targets, where the integral of dE/dx for the second pion was greatest. Only a few percent of the events contained a second passing pion, but the carbon elastic cross section is sufficiently large that these few percent overwhelmed the number of elastic proton events. The use of thin targets and this method of cutting the doubles content of the beam and scattering events with a pulse height restriction on S made possible the analysis of the six extreme small angle data points reported for this experiment (one data point at each energy and polarity).

V. THE CROSS SECTIONS

Final cross sections for the active target experiment are listed in Table III. Only data from near-optimum configurations were used in the final analysis. Cross sections were calculated as averages of single-target results, both from dual- and single-target data runs using

$$\frac{d\sigma}{d\Omega} = \frac{Y \cdot \cos(\theta_T)}{d\Omega \cdot lt \cdot B \cdot f_\pi \cdot f_d \cdot D \cdot T(1 - \delta T/T)},$$

where Y is the yield, θ_T is the target angle, $d\Omega$ is the effective solid angle as generated by the Monte Carlo routine, T is the target thickness in p/cm^2, the terms f_π and f_d are the pion and doubles fraction of the beam, lt is the data acquisition system live time, B is the scaled beam count, and D is the correction for pion decay between the S counter and the target. The term δT represents the thickness of target surface from which protons can escape, so that $(1 - \delta T/T)$ represents the effective fraction of the target thickness, as generated by the Monte Carlo routine. A correction has been applied to each cross section for loss of recoil protons in the target due to nuclear reactions. This correction ranged from 0.0 to 1.7%, depending on the recoil proton energy.[20]

The uncertainties listed in Table III are statistical, and generally sufficient data were taken so that $1/Y^{1/2}$ was in the range of 0.01 to 0.03. Exceptions to this were the 45 and 30 MeV π^+ data, where the presence of the $^{12}C(\pi, 2p)$ absorbtion reaction interfered with clean extraction of data from dotplots. For 45 MeV π^+, where this interference was small, an additional 1.0–1.5% error was related to extraction of this background. For 30 MeV π^+ data, the dotplots were abandoned in favor of histograms as described earlier, and the associated statistical errors in the yields come from $(Y + 2B)^{1/2}$, where Y is the net peak area and B is the background under the peak. An additional 3% error was added in quadrature to account for the uncertainty in fitting the 30 MeV $\pi^+ p$ background at each angle.

All yield uncertainties were added in quadrature with the statistical 1% effective solid angle and 1% surface loss uncertainties from the Monte Carlo results, and the sum appears in the cross-section table for each data point.

Normalization errors (Δ in Table IIIfor a representative case include uncertainties in f_π, which were small at these energies due to the good TOF resolution of the beam particles (0.5%), f_d (0.3%), target thickness (1.5%), computer live time (0.1%), randoms(<0.1%), counter geometry (0.5%), counter efficiency (0.5%), target angle (1.0-1.5% for $50 \leq \theta_T \leq 64°$), and nuclear reaction losses of protons in the target (0.0-0.3%). The value of Δ for the 30 MeV $\pi^+ p$ cross sections includes a 3% addition in quadrature with the above terms to allow for possible systematic uncertainties in extracting the yields from the histograms. There is a ± 0.5 MeV uncertainty in the incident pion beam energy,[12] but no corresponding amount has been added to Δ or the statistical errors in Table III for this effect.

VI. CONCLUSIONS

find own in Fig. 9, the $\pi^- p$ data reported here are in good agreement with the Karlsruhe KA84 phase-shift analysis (PSA)[21] at all angles for all three energies measured. The only other large-angle $\pi^- p$ differential cross section measurements in this energy region are those of Frank *et al.*,[10] which are also in good agreement with the PSA. At smaller scattering angles, Wiedner *et al.*[22] have reported $\pi^- p$ cross sections at 55 MeV which are also in agreement with this PSA. The experimental $\pi^- p$ data base is thus consistent at these low energies.

For $\pi^+ p$, Fig. 9 shows that, while the PSA agrees reasonably well with the smallest-angle data reported here at 66.8 MeV, it is too high at back angles, and too high for all angles measured at 45 and 30 MeV. These conclusions are supported by the $\pi^+ p$ data of Frank *et al.*[10] at 30.0 and 49.5 MeV, and by the back angle $\pi^+ p$ data of Frank *et al.* at 69.6 MeV. The agreement of the present $\pi^+ p$ results with those of Frank *et al.* is good except at 69.6 MeV, where the data of Frank *et al.* are lower at the smaller scattering angles. The PSA curves are also higher than the recent small angle 55 MeV $\pi^+ p$ data of Wiedner *et al.*[22] for the largest angles measured (25 to $34°_{\text{c.m.}}$), and higher than the back-angle $\pi^+ p$ measurements of Auld *et al.*[23] at 47.9 MeV, which lie several standard deviations below the PSA. The consistency of the data reported here with that of two previous papers by this experimental collaboration using independent experimental techniques[8,9] is indicated by the agreement, within experimental uncertainties, of the 66.8 MeV angular distributions from the three experiments, as shown in Fig. 10.

On the other hand, the $\pi^+ p$ measurements of Ritchie *et al.*[24] and of Bertin *et al.*[11] are in reasonable agreement with the angular distributions generated from the PSA. While the shape of data of Ritchie *et al.* at 65 MeV is compatible with that reported here at 66.8 MeV, overall agreement of these two data sets would require a normalization adjustment of about 20%.

Although the P_{33} partial wave resonance occurs at an energy over 100 MeV higher than the present mesurements, the $\pi^+ p$ cross sections at the low energies considered here are still dominated by the P_{33} partial wave. The $\pi^+ p$ data presented here indicate that the P_{33} phase shift in the 30 to 70 MeV range of incident pion energies is not as large as predicted by the two widely used phase shift analyses.[7,21] This conclusion is now supported by six independent measurements (Refs. 8–10, 22, 23, and the present work). The dispersion relations used by the PSAs to generate the πN observables at low energies are based on data near and above the resonance energy. Since dispersion theory is generally considered to be reliable, these low-energy data may indicate a problem with the higher-energy differential and total cross sections. While the present results differ from previous phase-shift predictions, the direction of the difference is opposite to that which would bring the $\pi^\pm p$ scattering data base into agreement with s-wave scattering lengths based on the results of pionic atom studies.[1,25,26] Thus the discrepancy in the experimental value of the πN sigma term continues.

ACKNOWLEDGMENTS

We thank the technical and support staff of TRIUMF for their assistance, P. Siegel for his assistance and computer codes, and H. Chase for his able help with acquisition and replay of the data. M. Kohler also provided valuable assistance with data analysis. This work was supported in part by the United States Department of Energy and the Natural Sciences and Engineering Research Council of Canada.

References

*Now at TRIUMF, Vancouver, British Columbia, Canada V6T2A3
†Now at SAIC, Santa Clara, CA 95054
[1]M. P. Locher and M. E. Sainio, Phys. Lett. **213B**, 85 (1988).
[2]J. Gasser and H. Leutwyler, Phys. Rep. **87C**, 77 (1982).
[3]R. L. Jaffe, in *AIP Conference Proceedings 176; Intersections Between Particle and Nuclear Physics*, Conference Summary, (Rockport, ME, Gerry M. Bunce, Editor, 1988).
[4]European Muon Collaboration, Phys. Lett. B **206**, 364 (1988).
[5]S. J. Brodsky, J. Ellis, and M. Karliner, Phys. Lett. B 206, 309 (1988).
[6]P. J. Bussey, J. R. Carter, D. R. Dance, D. V. Bugg, A. A. Carter, and A. M. Smith, Nucl. Phys. **B58**, 363 (1973).
[7]R. A. Arndt and L. O. Roper, SAID on-line program, version SP89.
[8]J. T. Brack *et al.*, Phys. Rev. C **34**, 1771 (1986).
[9]J. T. Brack, J. J. Kraushaar, D. J. Rilett, R. A. Ristinen, D. F. Ottewell, G. R. Smith, R. G. Jeppesen, and N. R. Stevenson, Phys. Rev. C **38**, 2427 (1988).
[10]J. S. Frank *et al.*, Phys. Rev. D **28**, 1569 (1983).
[11]P. Y. Bertin *et al.*, Nucl. Phys. **B106**, 341 (1976).
[12]C. J. Oram, J. B. Warren, G. M. Marshall, and J. Doornbos, Nucl. Instrum. Methods **151**, 445 (1978).
[13]R. Madey, F. M. Waterman, A. R. Baldwin, J. N. Knudson, J. D. Carlson, and J. Rapaport, Nucl. Instrum. Methods **151**, 445 (1978).
[14]F. D. Becchetti, C. E. Thorn, and M. J. Levine, Nucl. Instrum. Methods **138**, 93 (1976).
[15]Bicron Corporation, Newbury, Ohio 44065.
[16]Galbraith Laboratories, Inc., Knoxville, TN, 37921-1250.
[17]Huffman Laboratories, Inc., Golden, CO 80403.
[18]GEANT Version 3.10, Data Handling Division, CERN DD/EE/84-1.
[19]REVMOC, C. Kost and P. Reeve, TRIUMF Design Note TRI-DN-82-28 December 9, 1987.
[20]D. F. Measday and C. Richard-Serre, CERN Yellow Report, CERN 69-17 (1969).
[21]KA84 PSA Solution of the Karlsruhe Group, as taken from SAID on-line program (Ref. 7).
[22]U. Wiedner *et al.*, Phys. Rev. Lett. **58**, 648 (1987).
[23]E. G. Auld *et al.*, Can. J. Phys. **57**, 73 (1979).
[24]B. G. Ritchie, R. S. Moore, B. M. Preedom, G. Das, R. C. Minehart, K. Gotow, W. J. Burger, and H. J. Ziock, Phys. Lett. **125B**, 128 (1983).
[25]J. T. Brack, PhD Thesis, University of Colorado at Boulder, 1989.
[26]E. Bovet, L. Antonuk, J.-P. Egger, G. Fiorucci, K. Gabathuler, and J. Gimlett, Phys. Lett. **153B**, 231 (1985).

Table 1 $CH_{1.104}$ target data for the active target experiment. All targets are of Bicron BC412, for which the manufacturer specifies a density of 1.032 g/cm^3 and a H/C ratio of 1.104. These numbers have been confirmed to 1% by two independent chemical analysis laboratories (see Refs. [16] and [17]).

Target #	Thickness		
	cm	g/cm^2	p/cm^{2}x10^{21}
1	0.646±0.003	0.667±0.003	33.8 ±0.2
2	0.363±0.003	0.375±0.003	19.0 ±0.2
3	0.173±0.002	0.178±0.002	9.03±0.09
4	0.085±0.001	0.087±0.001	4.42±0.05

Table 2 The various geometric configurations used for data acquisition and systematic tests. $R_{\pi 1}$ and $R_{\pi 2}$ are the radii to the $\pi 1$ and $\pi 2$ counters shown in Fig. 1. In addition to the variations listed, data were taken in both single- and dual-target mode, and $\pi 1$ thickness tests were performed. The counter arms were spaced by 10 degrees.

T_π(MeV)	Target		Radius		$\theta_\pi(^\circ_{lab})$
	Thickness(mm)	θ_T(deg)	$R_{\pi 2}$(cm)	$R_{\pi 1}$(cm)	Min:Max
66.8	3.63, 1.73	39.5	123.8	65.0	40:80
	6.46, 3.63	48, 50, 46	123.8	65.0	50:100
	3.63	54.5	123.8	65.0	90:140
	6.46, 3.63	64.6	123.8	65.0	90:140
45.0	3.63, 1.73	47.5	123.8	65.0	50:100
	3.63, 1.73	50.0	98.5	98.0	50:100
	3.63, 1.73	63.0	98.5	98.0	80:130
	3.63, 1.73	61.0, 64.2	123.8	65.0	90:140
	3.63, 1.73	67.0, 70.0	123.8	65.0	90:140
30.0	1.73, 0.85	55.0	123.8	65.0	60:110
	1.73, 0.85	50.0	123.8	65.0	50:100
	1.73, 0.85	50.0	97.7	47.0	60,80:100
	1.73, 0.85	50.0	97.7	none	70(only)

Table 3 The center-of-mass differential cross sections. Uncertainties shown at each angle represent counting statistics and statistical uncertainties in the effective counter solid angle and effective target thickness as determined by the Monte Carlo process. Uncertainties in the absolute normalization (Δ) are shown separately at each energy. The center-of-target pion energies T_π have an uncertainty of ± 0.5 MeV.

	π^+p			π^-p	
T_π(lab) (MeV)	$\theta_{c.m.}$ (deg)	$\frac{d\sigma}{d\Omega}_{c.m.}$ (mb/sr)	T_π(lab) (MeV)	$\theta_{c.m.}$ (deg)	$\frac{d\sigma}{d\Omega}_{c.m.}$ (mb/sr)
30.0	57.7	0.213±0.042	30.0		
(Δ = 3.6%)	68.6	0.258±0.020	(Δ = 2.0%)	68.6	0.263±0.010
	79.4	0.359±0.013		79.4	0.235±0.007
	89.8	0.427±0.017		89.8	0.193±0.005
	99.9	0.484±0.018		99.9	0.170±0.006
	109.7	0.575±0.024		109.7	0.145±0.004
45.0			45.0	58.2	0.322±0.006
(Δ = 2.2%)	69.2	0.360±0.009	(Δ = 2.2%)	69.2	0.255±0.004
	79.9	0.468±0.011		79.9	0.216±0.004
	90.4	0.588±0.013		90.4	0.179±0.003
	100.5	0.779±0.017		100.5	0.148±0.003
	110.2	0.931±0.022		110.2	0.125±0.003
	119.7	1.121±0.024		119.7	0.101±0.002
	128.9	1.320±0.028		128.9	0.080±0.002
	137.8	1.538±0.032		137.8	0.058±0.003
66.8	47.6	0.715±0.019	66.8		
(Δ = 2.2%)	59.0	0.750±0.020	(Δ = 2.2%)		
	70.0	0.803±0.019		70.0	0.332±0.006
	80.8	0.995±0.024		80.8	0.256±0.005
	91.2	1.213±0.028		91.2	0.194±0.004
	101.3	1.514±0.035		101.3	0.159±0.004
	111.0	1.840±0.041		111.0	0.115±0.003
	120.4	2.275±0.047			
	129.5	2.565±0.053			
	138.4	2.894±0.060			
	147.0	3.133±0.067			

Figure captions

1. Counter arrangement for the active target measurement. Data were gathered simultaneously at six scattering angles. All flight paths were in air. Incident particle identification was determined by rf-referenced TOF to S and proper pulse height in S. The active target was of scintillator plastic, and was oriented relative to the beam so as to minimize the escape of recoil protons, which were detected in coincidence with the scattered pions.
2. Light output for the particles of concern as a function of pion elastic scattering angle for 66.8 MeV incident pions. Protons and carbon ions are assumed to stop in the target, while the pions are assumed to pass through the target. The proton and carbon curves are thus independent of target thickness and angle, while the light output of the passing pion varies with target angle and thickness as indicated by the three dash-dot curves, which represent typical targets of the indicated thicknesses oriented at the labeled angles relative to the incident beam.
3. A histogram of the target signal in coincidence with a pion telescope at a scattering angle of $120^{\circ}_{\rm lab}$. The π^+ beam was tuned to an incident energy of 67 MeV.
4. An example of raw target pulse height vs. $\pi 2$ TOF dotplots used to extract yields, gathered at $T_{\pi+}$ =66.8 MeV and $\theta_\pi = 60^{\circ}$. Carbon elastic and inelastic events are at the lower left. Elastic pion-proton events have nearly this same TOF, but produce greater pulse height in the target due to the light output of the recoiling proton. $^{12}C(\pi, \pi p)$ and $^{12}C(\pi, 2p)$ events form the continuum.
5. A sample 30 MeV $\pi^+ p$ histogram of the target signal, used to extract yields. The scattering angle is $100^{\circ}_{\rm lab}$. $^{12}C(\pi, \pi p)$ and $^{12}C(\pi, 2p)$ events form the continuum. A typical fit to the continuum is shown by the solid line.
6. Target surface losses as a function of recoil proton energy, for two targets of different thicknesses, generated by the GEANT program. Pion scattering angle increases to the right. Each curve has a minimum at the proton energy corresponding to protons recoiling parallel to the target surface. For example, the lowest open circle corresponds to an 18 MeV proton recoiling in a 3.63 mm target with $(90 - \theta_p) \simeq \theta_T = 64.2^{\circ}$ for a pion scattering angle of $120^{\circ}_{\rm lab}$. There are four calculated points for $\theta_\pi = 90^{\circ}$ and for 100°.
7. Cross sections derived from targets differing in effective thickness. Corrections used are as in Fig. 6. Two targets of 3.63 mm and 1.73 mm thickness were used simultaneously (see text), with an incident π^- beam of 45 MeV. Also shown are cross sections calculated by the difference technique, for which the surface corrections cancel. The standard deviation for the points at each angle is 1.8% The curves are from the Karlsruhe KA84 PSA (Ref. 21) and the SAID program (Ref. 7).
8. Measured 45 MeV cross sections versus target angle. Squares indicate data taken at $90^{\circ}_{\rm lab}$; circles represent data at $100^{\circ}_{\rm lab}$. Solid symbols are from runs using a 0.173 cm target and have surface corrections varying from 4–24%, open symbols are from 0.363 cm target and corrections vary from 2–10%. Error bars are statistical only. Maximum variations of cross sections from the average at each angle are about 2.5%.
9. The $\pi^{\pm} p$ active target cross sections at 30.0, 45.0, and 66.8 MeV. The cross sections as predicted from the KA84 PSA (Ref. 21) are included for comparison. The error bars reflect statistical errors only.
10. Comparison of the $T_\pi = 67$ MeV $\pi^{\pm} p$ differential cross sections as measured in three separate experiments. The experimental methods are two-arm coincidence (Ref. 8) (circle), single-arm TOF (Ref. 9) (triangle), and the active target technique (this work, square). Circles and triangles should have an additional 2% normalization uncertainty added to the statistical errors shown. Additional normalization uncertainties for the active target data are 2.2%. The solid curve is from the SAID SP89 PSA (Ref. 7), and the dashed curve is from the Karlsruhe KA84 PSA (Ref. 21), as taken from the SAID SP89 program.

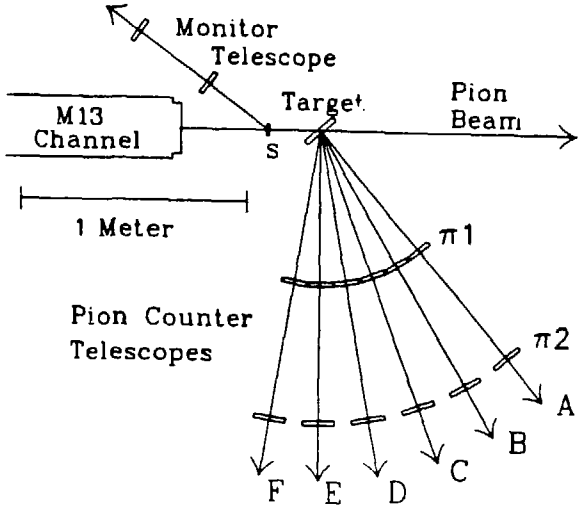

Fig. 1

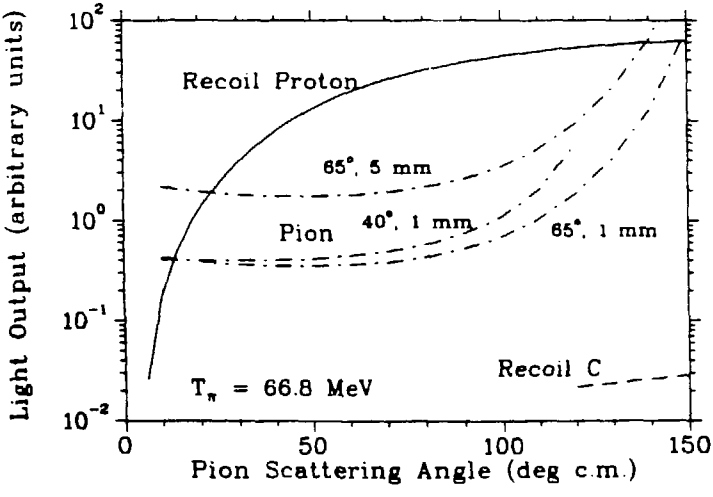

Fig. 2

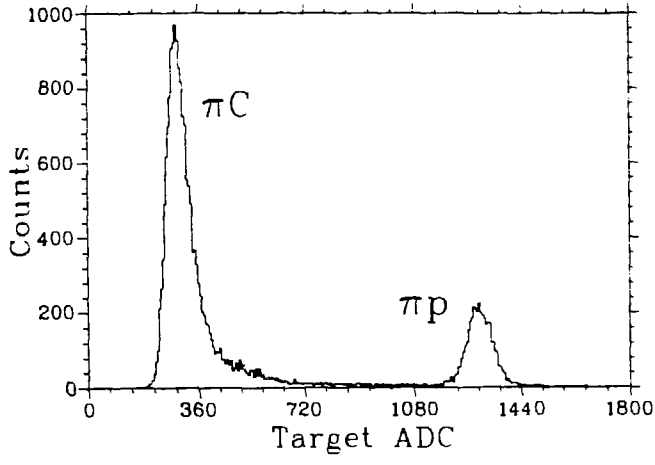

Fig. 3

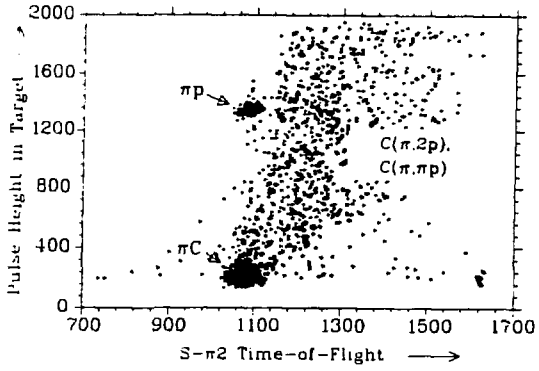

Fig. 4

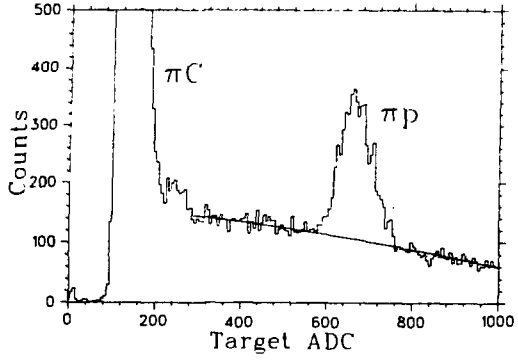

Fig. 5

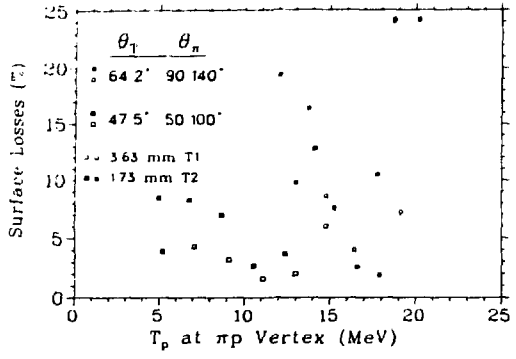

Fig. 6

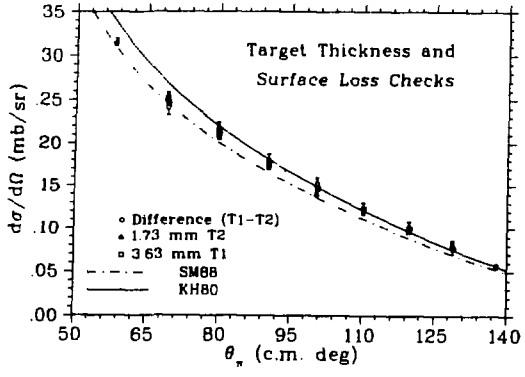

Fig. 7

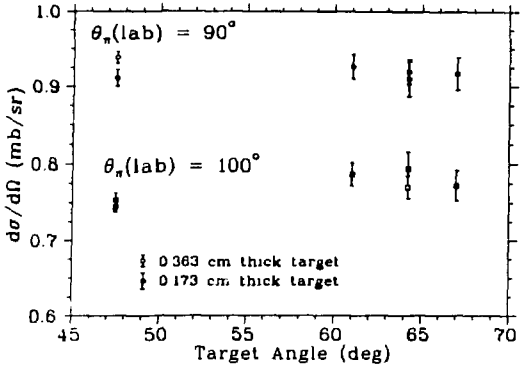

Fig. 8

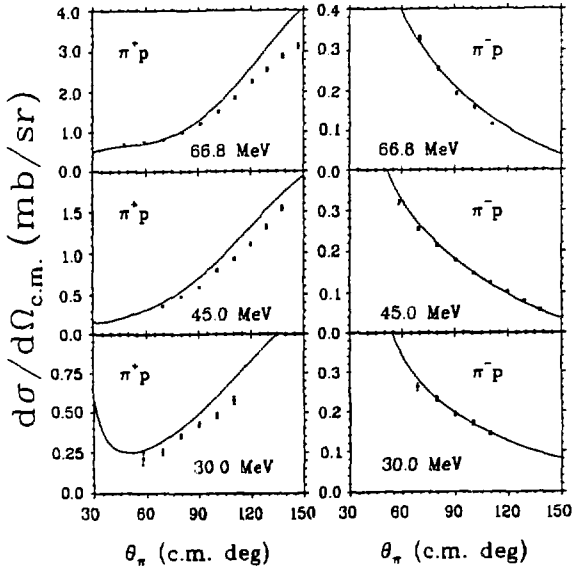

Fig. 9

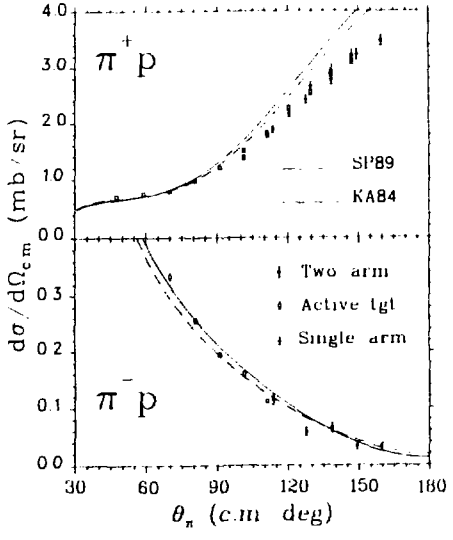

Fig. 10